2013-11-13

An Investigation into the Mechanisms of Formation of the Hard Zone in FSW X65

Jacob D. Allred
Brigham Young University - Provo

BYU ScholarsArchive Citation

Allred, Jacob D., "An Investigation into the Mechanisms of Formation of the Hard Zone in FSW X65" (2013). *All Theses and Dissertations*. 3806.
https://scholarsarchive.byu.edu/etd/3806

An Investigation into the Mechanisms of Formation of the Hard Zone in FSW X65

Jacob Allred

A thesis submitted to the faculty of
Brigham Young University
in partial fulfillment of the requirements for the degree of

Master of Science

Tracy W. Nelson, Chair
Carl D. Sorenson
David T. Fullwood

Department of Mechanical Engineering

Brigham Young University

October 2013

ABSTRACT

An Investigation into the Mechanisms of Formation of the Hard Zone in FSW X65

Jacob Allred
Department of Mechanical Engineering, BYU
Master of Science

Friction stir welding (FSW) of HSLA steel commonly produces a hard zone (HZ) on the advancing side (AS) of the weld. Despite its detrimental effects on weld toughness, the mechanisms of its formation have not been thoroughly investigated and are not well understood. This paper investigates the various mechanisms in FSW believed to affect the weld HZ, namely: strain, strain-rate, peak temperature and cooling rate. Gleeble tests indicate that strain and strain rate have negligible effects on weld HZ with cooling rate and peak temperature as dominant effects. Jominy tests resulted in cooling rate having 270% greater influence than peak temperature on the formation of lath ferrite microstructures similar to what is observed in the HZ of FSW X65. Comparing weld HZ microstructures to Jominy tests, it is estimated that cooling rates on the AS of the weld are at least 150°C/s higher than the retreating side. Reducing the cooling rate on the AS will likely lead to an improved microstructure at the weld HZ.

Keywords: hard zone, peak temperature, cooling rate, strain, strain-rate, lath ferrite, microstructure, FSW, HSLA, X65

ACKNOWLEDGMENTS

I would like to thank my committee for their guidance and direction on my research. I would especially like to thank my committee chair, Tracy Nelson, for his friendship and encouragement. I would also like to thank Jeff Farrer for his support and advice.

I would also like to thank my family for their encouragement and support throughout grad school. Most especially, I thank my supportive wife who was always willing to help and encouraging me to continue.

Funding for this work was provided by the National Science Foundation's Industry/University Cooperative Research Center Program and the Center for Friction Stir Processing under grant number IIP-0934377.

TABLE OF CONTENTS

LIST OF TABLES

LIST OF FIGURES

1 INTRODUCTION

High strength, low alloy (HSLA) steels are low carbon steels that have improved properties from a refined microstructure. Grain refinement is achieved through carefully controlled thermo-mechanical processing (TMCP) [1]. High strength, toughness, weld-ability and corrosion resistance make HSLA steels desirable for a large variety of industrial uses.

A majority of practical applications of HSLA steel use traditional arc welding for joining. Arc welding has been found to adversely affect the refined microstructure. Alternatively, friction stir welding (FSW) is a solid-state joining process that has been proven to provide superior post-process microstructure in HSLA steels [2-4].

Though FSW exhibits improvements in overall post-weld properties, a small-localized region of higher hardness, hard zone (HZ), has been observed on the advancing side (AS) of the weld. The HZ typically has a refined microstructure that may have an adverse impact on toughness and lead to premature failure in the weld [2, 5, 6]. FSW is a viable joining process; however there is limited understanding of the thermo-mechanical effects in FSW leading to the formation of the HZ.

This study provides an understanding of the effects of weld characteristics during FSW of HSLA X65 steel that contribute to the formation of the HZ.

2 BACKGROUND

Strength and fracture toughness of HSLA X65 is achieved through grain size refinement. Fine grains are obtained through thermo-mechanically controlled processing (TMCP). TMCP is a controlled rolling process that occurs at elevated temperatures, followed by accelerated cooling. Careful control is applied to the TMCP parameters to optimize the resultant microstructure for strength and toughness.

HSLA steels have various refined microstructural constituents. Microstructures of polygonal, acicular and lath ferrite have been observed in HSLA steels [7, 8]. Polygonal ferrite is typically polygonal or blocky in shape. In contrast, acicular ferrite exhibits less regular shapes and has various grain sizes with random orientations. Lath ferrite consists of narrow parallel growths that exhibits low angle misorientation between lath aggregates [9].

Most often joining of HSLA steel is accomplished via traditional arc welding, or fusion welding (FW). FW produces intense heat that melts metal in the weld zone. The high peak temperature in FW results in a decrease in toughness via grain coarsening, in particular in the heat affected zone (HAZ) of HSLA steel [10]. Numerous studies have attempted to mitigate grain coarsening in the HAZ by varying weld parameters and heat input [11, 12]. Despite these efforts, FW of HSLA steels continues to result in properties that exhibit reduced strength and toughness.

FSW is a solid-state joining process. Physical advantages include the benefit of single pass welds, low distortion and no loss of alloying elements [4]. FSW does not degrade weld quality as much as FW because weld temperatures remain below melting temperatures, avoiding the effects of solidification [3]. Often a majority of the post-weld microstructure maintains a refined microstructure similar to the TMCP base metal, retaining properties such as toughness and strength [2].

Frequently, FSW of HSLA steel exhibits microstructural differences across the weld. The weld zone, or stir zone (SZ), is primarily comprised of polygonal and coarse lath ferrite [2, 6]. In the HAZ, there has been no evidence of grain coarsening in FSW of HSLA steels [2, 8]. In the SZ, there is asymmetry in hardness, namely on the AS there is a region of higher hardness, the hard zone (HZ) [2, 8, 13, 14].

The HZ usually accounts for a small fraction of the overall area in the weld (Figure 2-1); however hardness values in the HZ can exceed the SZ by as much as 30% [5, 6]. The increase in hardness is due to grain refinement in the HZ which has been reported to typically comprise of lath ferrite [8, 14].

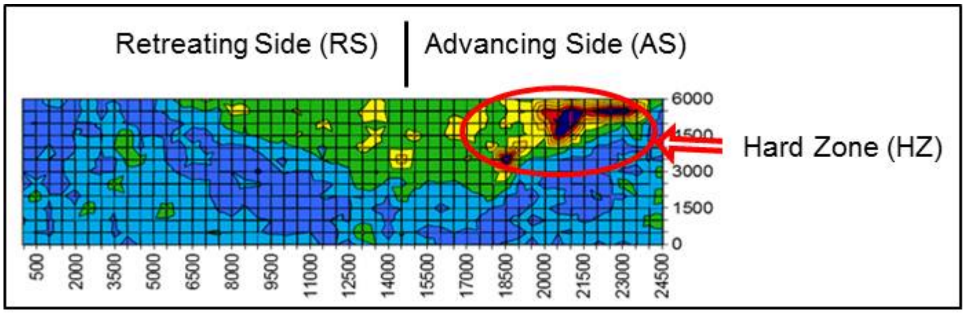

Figure 2-1: Vickers Microhardness Map FSW X65 (Hard Zone)

The HZ has been shown to have decrease in toughness compared to the rest of the weld [8]. This can degrade the quality of the weld and can be a source of premature failure. It has been reported that the decreased toughness in the HZ correlates to the microstructure. In particular, an increase in lath length resulted in a decrease toughness [15]. Thus, it is important to understand what are the underlying causes of lath ferrite formation during FSW of X65.

In FSW, deformation and friction between the tool and material around the tool are the main source of heat generation and strain. Variations in the weld microstructures have been found to correlate with FSW parameters [8, 14]. In particular, the weld HZ has been reported to vary with weld parameters [16]. This indicates that weld parameters may correlate to specific weld microstructures. However, due to the high plastic deformation, there are limitations in measuring weld heating rates, strain, strain-rate and cooling rates known to affect HSLA steel microstructure.

It is common to estimate weld characteristics through simulations and interpretation of available data. Deformation, or strain and strain-rate, is commonly estimated via numerical simulations, resulting in large variations of reported values due to the large number of unknowns. Strain values for various weld parameters have been estimated from 5.2 to 50 and strain rates from 100 s^{-1} to 1000 s^{-1} [17-20]. Because direct measurement of heating rates and cooling rates are prohibitive during FSW, temperatures are commonly extrapolated from thermocouple measurements in the HAZ [21, 22] or tool [8, 23]. Peak temperatures in FSW of steels have been estimated above 1000°C, typically ranging from 1000°C to 1350°C [8, 13, 21, 22].

FSW is commonly compared to an extrusion process in which the flow of material around the tool is compared to other TMCPs [24-27]. It is believed in FSW that strain (or deformation) plays a significant role in refining weld microstructure through recrystallization (RX) in aluminum alloys [28-30], HSLA steels [14, 31], stainless steels [3, 32] and other materials [23, 33]. As with any TMCP process, significant factors affecting microstructure in FSW are heating and cooling rates.

Material properties of HSLA steels are highly dependent upon the post TMCP microstructure. Deformation and thermal characteristics are carefully controlled and monitored to provide an optimized microstructure. In particular, thermal parameters have been found to have large influence over the properties of HSLA steel [34].

For example, an increase in cooling rate results in the reduction of grain size and an increase in the volume of acicular and lath ferrite [35], potentially resulting in an increase in strength and a decrease toughness [36]. Deformation rolling above the austenite recrystallization temperature reduces the prior austenite grain (PAG) size, which has been shown to increase toughness as well [37].

Recent work has reported that peak temperature may have a predominate effect on weld microstructure in FSW of steel [21, 22]. Pilchak hypothesized that temperature plays a dominate role in FSW of titanium [23]. However, no data was provided correlating temperature (or strain) to resultant microstructures. Matsushita and Sinfield reported successful simulation of the SZ in steel and concluded that peak temperature plays a predominate role over strain in the resulting microstructure [21, 22]. Matsushita suggested further investigation of the effects of strain and did not investigate the effects of other weld characteristics, namely: cooling rate, strain rate, and time above transition temperatures. Sinfield did not fully investigate the range of cooling rates that are likely present in FSW of HSLA steel, and inconclusive data correlating values of weld characteristics to resultant microstructure were provided.

To better understand the formation of weld microstructure and in particular the HZ, further investigation into the effects of weld characteristics is needed. Many FSW studies measure and discuss effects of post-weld microstructure in relation to weld parameters, but few have addressed interaction of weld characteristics and their effect on weld microstructure. Further, limited research has investigated the effects of weld characteristics on the formation of the HZ in FSW of HSLA steels.

The purpose of the present work is to identify the mechanisms which lead to the formation of the HZ in FSW X65. An investigation into the effects of FSW characteristics on the microstructure of HSLA X65 will lead to a better understanding of the formation of the HZ. Significant weld characteristics, namely strain, strain-rate, total time above A_3 transition temperature, cooling rate and peak temperature are simulated using Gleeble hot torsion and Jominy end quench testing.

3 EXPERIMENTAL APPROACH

3.1 Material

12.7mm thick HSLA X65 steel plate was used in this study. Samples for welding, Gleeble and Jominy testing were obtained from the same rolled plate. The chemical composition is found in Table 3-1.

Table 3-1: X65 Chemical Composition

C	Mn	P	S	Si	Ni	Cr	Mo	Cu	Al	V	Nb	Ti	N		CE
0.054	1.26	.005	<0.005	0.286	0.163	0.028	0.005	0.303	0.028	0.03	0.05	0.013	0.007		0.31

The transition temperatures were found using equations (1) and (2) below. Ac_1 and Ac_3 equations are valid equations for steels with less than %0.6 Carbon Equivalent (CE) [38]. Using the composition of X65 found in Table 2-1, the calculated Ac_1 is 715.5°C and Ac_3 is 818.8°C. Ac_1 is the temperature at which austenite begins to form and Ac_3 is the temperature when the material is fully austenite. Test temperatures above Ac_3 were used to ensure full austenitization of material while testing.

$$\mathbf{Ac_1(C)} = 723 - 16.9Ni + 29.1Si + 6.38W - 10.7Mn + 16.9Cr + 290As \tag{1}$$

$$\mathbf{Ac_3(C)} = 910 - 203\sqrt{C} - 15.2Ni + 44.7Si + 104V + 31.5Mo + 13.1W \tag{2}$$

3.2 Friction Stir Welding

Welds were performed on a TTI FSW machine with a CS4 E44111 tool from Megastir (Appendix A- Figure A-1). Bead-on-plate welds were used with 0° head tilt.

In this study welding variables were tool rotation speed (RPM) and travel speed (or inches per minute - IPM). There were three different weld parameters used that resulted in three different HZ measurements (Table 3-2). Consistent with available literature, the HZ was defined as any localized hardness that exceeded 10% of the average weld hardness [2, 8, 13].

Table 3-2: FSW Parameters

Weld	IPM	RPM	TOTAL AREA HZ (mm^2) (Hardness > 250 Vickers)
A	7	260	2.25 mm^2
B	3	260	0.75 mm^2
C	7	400	2.75 mm^2

3.3 Modified Gleeble Torsion Test

This study used a modified Gleeble sample for hot torsion testing (Appendix A – Figure A-2) [39]. A Gleeble 3500 Universal Testing System was used to perform hot torsion tests. The design of the modified Gleeble samples allowed internal and external cooling, providing a more uniform quench.

Gleeble physical simulation allows the exact reproduction of the thermal and mechanical processes in the laboratory that the material is subjected to FSW. Gleeble testing allow independent control of variables such that material follows the same thermal and mechanical profile that would be expected during FSW.

Independent control of each physical variable allows accurate simulation of proposed FSW characteristic. During testing the specimens undergo a specified plastic deformation at a specific rate, after being heated to a specified peak temperature. The test also allows for prolonged periods at peak temperature, after which a specific cooling rate is achieved using an adjustable quench medium (gas or water mist).

All variables were controlled and monitored through the Gleeble data acquisition system. Each specimen was allowed to reach the ferrite-austenite transformation temperature before introducing strain. Temperatures were increased in the gage section of each sample through resistive heating. One Type-K thermocouple was welded to the center of each sample to measure temperature. Cooling rates were controlled through either helium or water mist quench.

Gleeble tests investigated five (5) variables that are characteristic of FSW: peak temperature, strain, strain rate, cooling rate and time above A_3 transition temperature. Two design of experiments (DOE) were used in testing the significance of the 5 variables.

The first experimental design was a small composite design (SCD) that investigated control variables: strain, strain rate, cooling rate and peak temperature. The SCD adds star points (alpha points, α=1.414) to clear the main effects of aliasing with the two-factor interactions, while enabling a reduction in the number of runs required. Run order was randomized before testing began. Cooling was achieved using a helium quench.

The ranges for each of the variables are shown in Table 3-3 below. These values were selected based on current understanding of FSW characteristics in HSLA steel. Peak temperatures in FSW of steel have been estimated from 1000°C to 1350°C [8, 13, 21, 22]. Cooling rates in the HAZ have been measured over 40 C/s with higher expected cooling rates in the weld [8]. Numerical simulations have predicted deformation, or strain from 5.2 [19] to 50 [20] for various steels and strain rates of 100 s^{-1} [18] and 1000 s^{-1} [17]. The full DOE for these variables is listed in Table B-1in Appendix B.

Table 3-3: Small Composite Design of Experiment

VARIABLE	HIGH	LOW
Strain	2	1
Strain Rate	0.119sec^{-1}	1.194sec^{-1}
Peak Temp	850 C°	1050 C°
Cooling Rate	4 C°/s	16 C°/s

The second experimental design was a 2^k factorial design that was aimed at increasing the range of cooling rates and times above A_3 temperature. Compared to the SCD, the 2^k experimental design resulted in a larger range of cooling rates. Cooling rates were achieved using an external water mist quench.

The ranges for the 2^k experiment control variables are shown in Table 3-4 below. Strain and strain rate were held constant as 1.5 and 0.7 sec^{-1}, respectively. Time above the transition temperature was varied to simulate longer or slower dwell times during welding. The full DOE for the 2^k factorial design variables is listed in Table B-2 in Appendix B.

Table 3-4: 2^k Design of Experiment

VARIABLE	HIGH	LOW
Cooling Rate	126.33 C°/s	27.3 C°/s
Peak Temp	1100 C°	900 C°
Time Above A_3	300 sec	10 sec

Peak temperature, cooling rate and time above transition temperature were all measured directly using the Gleeble data acquisition system. Cooling rates were measured from 800 to 500°C.

The strain was not uniform across the entire gauge section of Gleeble samples. Strain (strain-rate) calculations were performed using one-half (½) the gauge length. Resistive heating was used that results in a temperature gradient with the highest temperatures concentrated at the center of the sample. Higher temperatures reduce flow stress, which was the result of non-uniform deformation, with the highest deformation concentrated in the center-most section of the gauge area [40]. Sinfield reports similar findings in Gleeble tests [22].

To illustrate the non-uniform strain, indentations were stamped into a test specimen prior to testing (Figure 3-1). Post testing, indents along the center half of the gauge underwent the largest deformation. The distance between indents and the indent strained-ellipse major axis length were the largest at the center half. Minimal differences could be determined between the points in the center half, thus the center half of the gauge section was used for calculations and analysis.

Figure 3-1: Gleeble Sample Localized Strain

The shear strain (ϒ) was calculated using the following equation:

$$\gamma = \frac{r \cdot \theta}{l} \tag{3}$$

Where $\boldsymbol{r}$ is the modified Gleeble gauge section outside radius, $\boldsymbol{\theta}$ is the desired rotation in radians for each specific specimen, and $\boldsymbol{l}$ is half the length of the gauge section.

The strain rate **($\dot{\Upsilon}$)** was converted into revolutions per minute (RPM) using the following equation solving for revolutions per minute, $\boldsymbol{\dot{\theta}}$:

$$\dot{\gamma} = \frac{r \cdot \dot{\theta}}{l} \tag{4}$$

3.4 Microhardness and Metallographic Examination

One metallographic sample was extracted from each hot torsion sample. The sample gauge section was removed using a cooled abrasive. A lateral cut was made along the long axis of each gage section using a low speed diamond saw. This method prevented any heat generation or large deformation that could affect the post-process microstructure and material properties.

The samples were then mounted in 38.1 mm (1.5 in) diameter Glass Filled Epoxy molds and then ground and polished through a series of silicon carbide abrasive disks and alumina, respectively. Final polishing was done using 0.05 µm colloidal silica on a vibratory polisher.

Metallographic samples were removed from each of the FSW X65 welds using a transverse cross-section perpendicular to weld path. Samples were removed using a waterjet and then mounted in 38.1mm (1.5in) diameter bakelite molds and polished similar to Gleeble specimen polishing.

After analyzing the hardness profile, the Jominy specimens were reduced in length to 31.75mm (1.25in) starting at the quench end. For metallographic analysis, the specimen was cut longitudinally along the sample axis using a wire EDM, mounted and polished similarly to Gleeble torsion specimens.

To quantify sample microstructure changes, all metallographic samples were prepared for electron back-scatter detection (EBSD) analysis. EBSD scans were performed using a FEI XL-

30 SFEG scanning electron microscope (SEM) equipped with TSL 5.2 OIM data collection software. The SEM beam voltage and spot size were 20 KV and 6.

EBSD scans were performed using a hexagonal grid at the area of interest for each test specimen. Gleeble scans were performed on the outermost edge of the specimens in the geometric center of the gauge section, as highlighted in red in Figure 3-2. For Gleeble samples, a hexagonal grid of 50 µm x 50 µm with a step size of 0.15 µm was used. For weld specimens, a scan at the HZ was performed with a hexagonal grid of 200 µm x 200 µm with a step size of 0.3 µm. The location of the HZ was determined using microhardness plots. Jominy scans were along the centerline of the sample with a hexagonal grid of 100 µm x 100 µm with a step size of 0.3 µm.

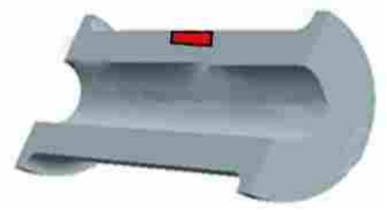

Figure 3-2: Gleeble Torsion

All microhardness data was acquired from the same metallographic samples used for microstructural analysis. The microhardness testing was performed using the Leco LM100AT Microhardness Tester, which included the AMH43 software. For the weld samples, a grid of indents was created to encompass the entire weld area and the surrounding base metal. This allowed identification of HZ and SZ for later microstructural analysis. Microhardness for the jominy end quench specimen was performed per ASTM A255 standard. All of the microhardness data is displayed as a contour map generated by Matlab.

3.5 Microstructural Characterization

TSL OIM software was used to measure both grain size area and all high angle grain boundaries. Consistent with previous work in HSLA steels, grain boundary (or bainite/lath packet) angles were defined as any misorientation angle greater than or equal to 15° between neighboring points. Any misorientation less than 2° was difficult to determine due to the selected scan resolution. Thus, lath boundaries were defined as low angle misorientation from 15-2°.

Aspect ratio was measured using image analysis with Matlab. From the EBSD data, a misorientation map (Figure 3-3a) was created that contained outlines of all misorientation angles great than 2°. This was converted to a binary image and then analyzed to identify all boundaries. The boundaries defined all the contained shapes in the misorientation map. Each shape was measured for the major and minor axis and fit with an ellipse that was used to determine the resultant aspect ratio (Figure 3-3b).

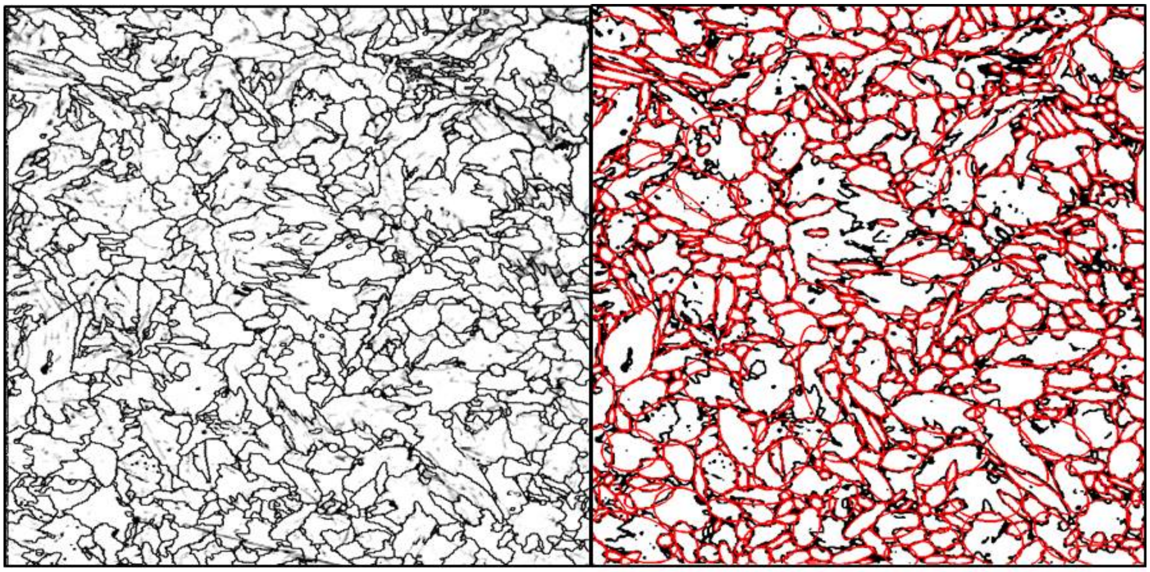
a: Misorientation Outline

b: Ellipses around grains/lath structures

Figure 3-3: Grain Map with Aspect Ratio Measurements

3.6 **Jominy End Quench**

A modified jominy end quench was used to test the effects of peak temperature and cooling rates on X65 microstructure with no effects from strain and strain rate. In order to maintain consistency in chemical composition, the same ¾” plate material that was used for weld testing and Gleeble tests was utilized for Jominy tests. This resulted in a modification of the dimensions of the standard Jominy specimen with a decrease in diameter of 25% from the ASTM A255 standard (1” diameter). Full dimensions of the modified jominy specimen can be found in Appendix A - Figure A3. It is well known that Jominy heat flow in the center of the sample (location of analysis) is considered 1-dimensional flow. It is assumed that the modification to the sample diameter does not significantly affect the testing or analysis. Testing methods and measurements were performed per the standard ASTM A255 [41].

Jominy end quench tests were performed at three (3) different peak temperatures: 900, 1000, 1100°C. Jominy cooling rates are described as a function of distance from quench end (Figure 3-4). Cooling rates in Figure 3-4 have been previously developed for steel Jominy tests [42, 43], thus this cooling curve was used in this study. This will be used to evaluate microstructure as a function of cooling rate for Jominy samples.

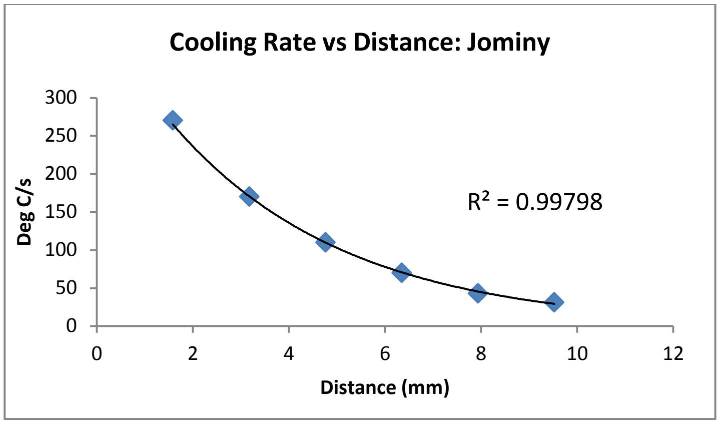

Figure 3-4: Cooling Rates for Jominy End Quench

EBSD scans were performed along each Jominy sample centerline at 1mm, 2mm, 4mm and 8mm from the quench end. Increasing logarithmic distances were selected to capture the exponential decrease/increase grain growth with increasing and decreasing temperature in steels. Table 3-5 summarizes the peak temperatures and cooling rates that were analyzed in this study.

Aspect ratio for the scans at 1mm in all Jominy tests was difficult to determine due to the very fine microstructural features. To determine the 1mm scan average aspect ratio, a best-fit curve was fit to the 2mm, 4mm and 8mm scans with continuation of this line represented by a dashed line for the 1mm scans (Figure 3-5).

To verify the accuracy of the best-fit line, for each Jominy sample aspect ratios of two randomly selected areas in the scans at 1mm were compared to the best-fit line. These random areas account for 30% of the scan area. The largest difference between the predicted aspect ratio and the sample area measured area aspect ratio was ~5% for the 1100°C sample. The complete microstructural data for all Jominy samples can be found in Table 3-5.

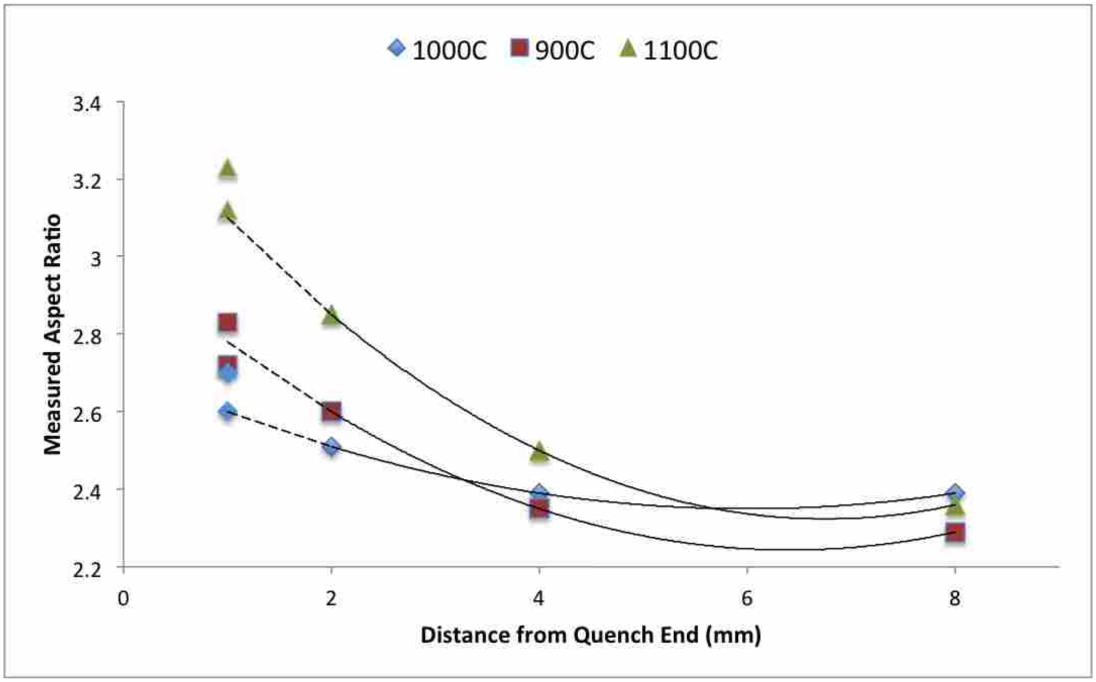

Figure 3-5: Jominy AR Measurements

Table 3-5: Jominy End Quench Results

Location	**Cooling Rate (distance)**	**Aspect Ratio**			**Fraction HAGB**		
		900	**1000**	**1100**	**900**	**1000**	**1100**
Random area A	312°C/s (1mm)	2.72	2.6	3.23	0.458	0.389	0.432
Random area B	312°C/s (1mm)	2.83	2.7	3.12	0.458	0.389	0.432
Predicted	312°C/s (1mm)	2.78	2.6	3.1	N/A	N/A	N/A
Measured	237°C/s (2mm)	2.6	2.51	2.85	0.531	0.494	0.420
Measured	136°C/s (4mm)	2.35	2.39	2.5	0.602	0.552	0.518
Measured	45°C/s (8mm)	2.29	2.39	2.36	0.683	0.562	0.534

4 RESULTS AND DISCUSSION

Gleeble test values and associated resulting microstructure measurements for both experimental designs are shown Table 4-1.

Table 4-1: Hot Torsion Variable Values and Test Results

DOE	Sample	PARAMETERS				RESPONSES			
		Peak Temp (°C)	Cooling Rate (°C/s)	Strain	Strain Rate	Fraction Bainite	Fraction Misorientation Angle		Ave. Grain Area
						%	2°-15°	15°+	um^2
SCD DOE	1*	950	12	1.5	0.66	1.3	0.31	0.69	97.0
	2	1000	10	1.75	0.93	1.6	0.45	0.55	86.5
	3	950	4	1.5	0.66	0.2	0.25	0.75	138.2
	4	950	18	1.5	0.66	3.3	0.41	0.60	58.8
	5	900	16	1.75	0.39	2.4	0.25	0.75	37.5
	6	900	12	1.25	0.93	0.8	0.26	0.74	42.8
	7	1050	15	1.5	0.66	1.1	0.56	0.58	66.3
	8	950	12	2	0.66	2.6	0.20	0.80	92.5
	9	950	13	1	0.66	1.7	0.21	0.79	78.7
	10	950	15	1.5	0.12	2.4	0.17	0.83	48.7
	11	1000	16	1.75	0.93	2.0	0.33	0.67	86.2
	12	900	15	1.25	0.93	3.4	0.12	0.88	42.9
	13	950	14	1.5	1.19	2.4	0.31	0.69	80.0
	14*	950	13	1.5	0.66	1.2	0.14	0.86	58.6
	15	1000	17	1.25	0.39	1.2	0.29	0.71	111.9
	16	900	11	1.75	0.39	1.1	0.16	0.84	36.9
	17	1000	12	1.25	0.39	0.9	0.30	0.70	104.2
	18	850	12	1.5	0.66	2.9	0.17	0.83	35.1

	Sample	PARAMETERS					RESPONSES			
		Peak Temp (°C)	Cooling Rate (°C/s)	Time Above A_3 (sec)	Strain	Strain Rate	Aspect Ratio	Fraction Misorientation Angle		Ave. Grain Area
							Average	2°-15°	15°+	um^2
2^k DOE	0	900	55	300	1.5	0.66	1.96	0.26	0.74	34.4
	1	1100	64	10	1.5	0.66	2.90	0.55	0.45	130.6
	2	1100	126	300	1.5	0.66	2.96	0.59	0.41	124.2
	3	900	31	10	1.5	0.66	2.02	0.22	0.78	40.3
	4	900	27	300	1.5	0.66	1.84	0.29	0.71	43.0
	5*	1000	45	155	1.5	0.66	2.51	0.48	0.53	104.9
	6	1100	110	10	1.5	0.66	3.22	0.56	0.34	101.4
	7	900	88	10	1.5	0.66	2.2	0.23	0.77	60.3
	8*	1000	62	155	1.5	0.66	2.27	0.41	0.60	127.9
	9	1100	87	300	1.5	0.66	2.84	0.62	0.38	186.3

* Center Repeats

Changes in polygonal ferrite were best characterized using the total fraction volume of bainite and grain size (total area). Bainite observed in SCD testing was similar to bainite islands in base metal of HSLA steel [44]. EBSD resolution and small islands with fine lath structures limited bainite analysis to calculating the total area fraction of bainite islands. As expected, grain size was particularly useful in describing microstructural changes in polygonal ferrite.

Not all quantitative microstructural characteristics that were analyzed were accurate in describing lath ferrite microstructures. Because the weld HZ contains large fractions of lath ferrite, determining accurate simulation of lath ferrite requires capturing changes in lath ferrite and in particular lath characteristics that are known to affect toughness.

As previously mentioned, a decrease in toughness is associated with an increase in lath length (or effective grain size). The best method to capture changes in the effective grain size is by measuring aspect ratio (length to width) of each lath structure. An increase in lath structures is also known to be associated with decreasing neighboring boundary angles [9]. Thus, both the fraction of high angle grain boundaries (HAGB) and aspect ratio were most effcective in evaluating lath ferrite characteristics.

4.1 **Gleeble Simulation of Weld HZ**

Gleeble samples were successful in simulating a range of microstructures, Figure 4-1a through c. The SCD Gleeble test resulted in primarily polygonal ferrite (Figure 4-1c) and the 2^k experimental design resulted in a range of polygonal to 89% lath ferrite (Figure 4-1a).

The 2^k samples with high fractions of lath ferrite were found to have quantitative and qualitative similarities to the HZ microstructures found in FSW HSLA X65. The fraction of lath ferrite in 2^k Gleeble sample #2 (Figure 4-1a) resembled weld HZ A (Figure 4-1d) with 89% and 84% lath ferrite, respectively. Table 4-2 shows a quantitative comparison of microstructural characteristics for several Gleeble samples and weld HZs with similar fractions of lath ferrite and aspect ratios.

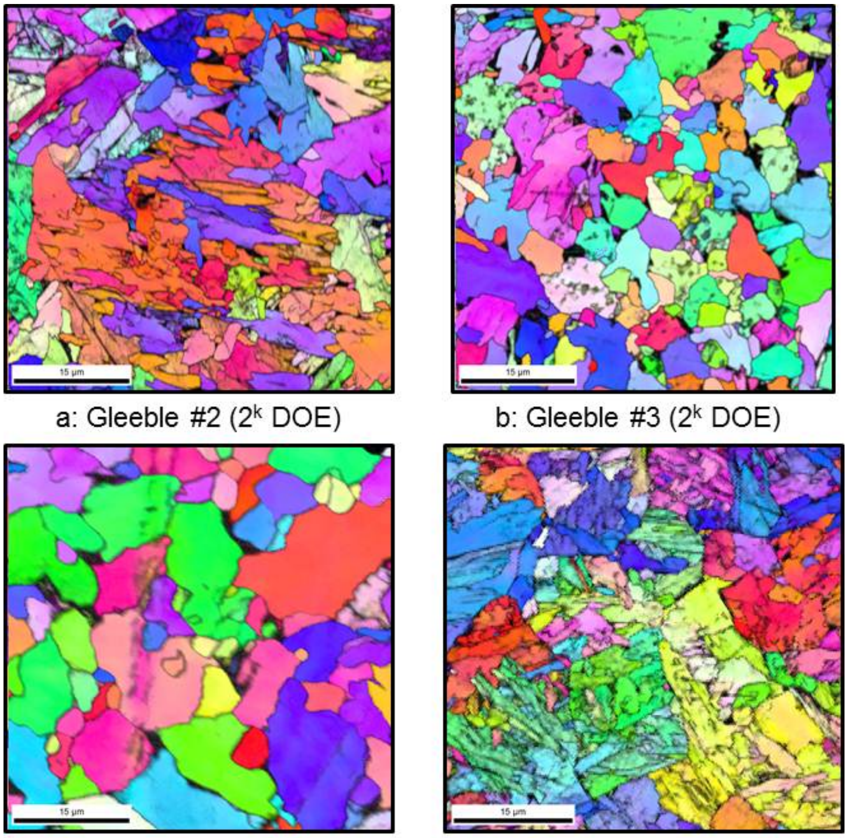

a: Gleeble #2 (2^k DOE) b: Gleeble #3 (2^k DOE)

c: Gleeble #1 (SCD) d: Weld A

Figure 4-1: Gleeble and Weld HZ Microstructure Transition Polygonal to Lath Ferrite

Table 4-2: Weld – Torsion Comparison

	Average Aspect Ratio	Fraction High Angle Boundaries
Weld A	2.89	0.37
Gleeble - #2 (2^k DOE)	2.96	0.41
% Difference	2.4%	9.1%
Weld B	2.42	0.46
Gleeble - #5 (2^k DOE)	2.4	0.53
% Difference	0.8%	15.2%
Weld C	2.38	0.628
Gleeble - #8 (2^k DOE)	2.27	0.60
% Difference	4.8%	4.4%

4.2 Gleeble Statistical Results

To fully characterize the effects of Gleeble parameters (Table 4-1) on resultant microstructure, a statistical analysis was performed for both experimental designs. Two screening criteria were used to determine statistical significance. All terms in the statistical models that resulted in a p-value greater than 0.05 were discarded. It was predetermined that all responses (Table 4-1) that resulted in a fit (R^2) of less than 40% would be discarded, however as discussed later all responses resulted in an acceptable fit.

The results from the statistical analysis of the SCD are found in Table 4-3. As shown, there was a poor fit for a majority of the responses, however peak temperature and cooling rate were found to have the largest influence of all variables. There were no interaction terms that were found to have statistical significance. Details of these findings will be discussed in further detail in subsequent sections.

Table 4-3: SCD ANOVA Results

Response	R^2	P-Value			
		Peak Temperature *p-value (coefficient)*	Cooling Rate *p-value (coefficient)*	Strain	Strain-Rate
Fraction Bainite	0.54	**0.019 (-0.0086)**	**0.003 (0.182)**	0.196	0.283
Boundary Angles 2-15°	0.51	**< 0.001 (0.0017)**	0.728	0.563	0.192
HAGB (15°+)	0.46	**< 0.002 (-0.00135)**	0.758	0.558	0.186
Grain Size (um^2)	0.59	**< 0.001 (0.405)**	**0.003 (-4.686)**	0.467	0.900

Responses from the 2^k statistical analysis (Table 4-1) were all found to have an acceptable fit. The resultant statistical models for the responses grain size and aspect ratio are found in equations 5 and 6 below. Models for grain boundary angles are not discussed in detail, because HAGBs were found to proportionally decrease with increasing aspect ratio. This is expected as an increase in lath aggregates results in an increase in grain aspect ratio and an increase low angle misorientations [10, 45].

Each significant term included in the statistical models (eq. 5 and 6) exhibit various levels of influence on the response. This is determined by the magnitude of the coefficients (independent or interaction), with greater magnitude corresponding to higher influence.

$$\text{Grain Size (um}^2\text{)} = 96.3 + 73.2*(PT) - 25.5*(CR) + 1.03*(TA_3) + 34.2*(PT*TA_3) - 37.5*(CR*TA_3) \tag{5}$$

$$R^2 = 0.962$$

$$\text{Grain Aspect Ratio} = 2.49 + 0.42*(PT) + 0.17*(CR) - 0.09*(TA_3) \tag{6}$$

$$R^2 = 0.973$$

*All Variables are Normalized

To better understand which Gleeble parameters affect lath ferrite formations, each of the variables is discussed in detail in the following sections.

4.2.1 Strain – Strain Rate

For the ranges investigated, strain and strain-rate were found to have no effect on the morphology of microstructure. As indicated in Table 4-3, results from the SCD conclude that the tested values for strain and strain-rate have no statistical significance. All terms relating to strain and strain-rate in the statistical responses were found to have p-values greater than 0.05. Matsushita reported similar findings that strain has negligible effects in HSLA steel microstructure [21].

4.2.2 Thermal Variables

Time above A_3 transition temperature (TA_3) was statistically significant but has limited influence for small values. The coefficients in equations 5 and 6 indicate that independently, TA_3 had a less than 1% influence on grain size and less than 18% influence on aspect ratio. In equation 5, if TA_3 values approach 60 seconds, the interaction terms have less than 10% influence on grain size.

In FSW, for even low IPM values, the total time the weld material is above the A_3 temperature is likely not to exceed 60 seconds. Therefore, it is expected that for FSW X65, TA_3 has minimal influence on the formation of lath ferrite in X65 HSLA steel. While varying peak temperature 100°C (1150-1250°C) and soaking time (TA_3) 1 to 5 min in HSLA 100, Dhau similarly reports that soaking time had significantly less influence on the PAG size than peak temperature [46].

Peak temperature and cooling rate have the greatest influence on X65 microstructure morphology. The response surface plots below show grain size and aspect ratio as a function of peak temperature (Figure 4-2a) and cooling rate (Figure 4-2b), respectively. A 22% increase in peak temperature (900-1050°C) and a 367% increase in cooling rate (27-126°C/s) resulted in a 73% increase in aspect ratio (1.81-3.13). Similarly, a 22% increase in peak temperature and a 367% decrease in cooling rate resulted in a 350% increase in grain size (52.8 µm-185.2µm).

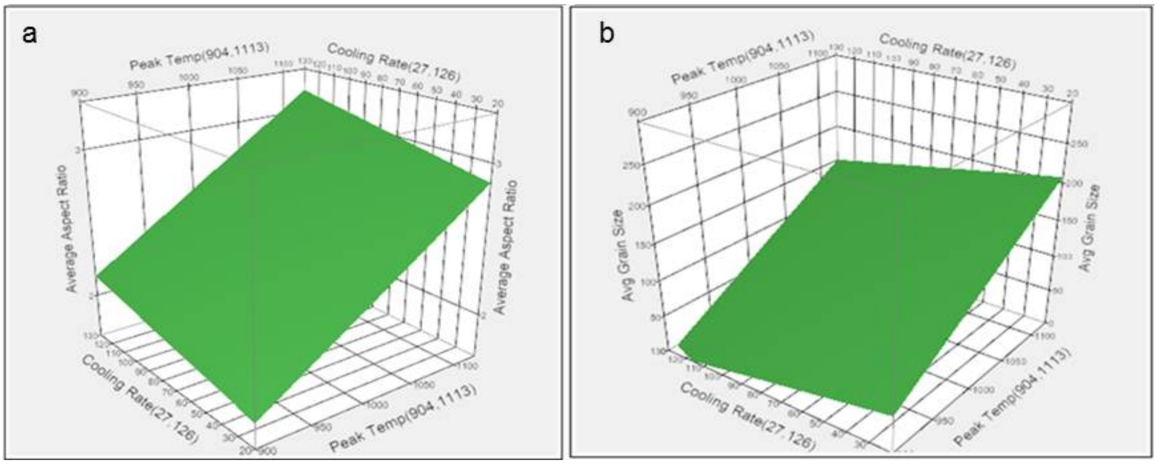

Figure 4-2: a) Aspect Ratio and b) Grain Size Response Surfaces

4.2.2.1 Peak Temperature

Figure 4-3 shows EBSD scans of Gleeble samples #7 and #9 from the 2^k DOE. These samples had a difference in peak temperature of 200°C: cooling rates (88°C/s and 87°C/s respectively), strain and strain rates was held constant. A 200°C difference in peak temperature resulted in a 30% increase in aspect ratio, a 51% decrease in HAGB and 209% increase in grain size.

The increase in lath ferrite with increasing peak temperature is likely due to change in the PAG size. Shome, Dhau and others have found that increasing peak temperature results in an increase in PAG size [9, 47-49]. Larger PAGs produce higher fractions of lath and acicular microstructures [9,49].

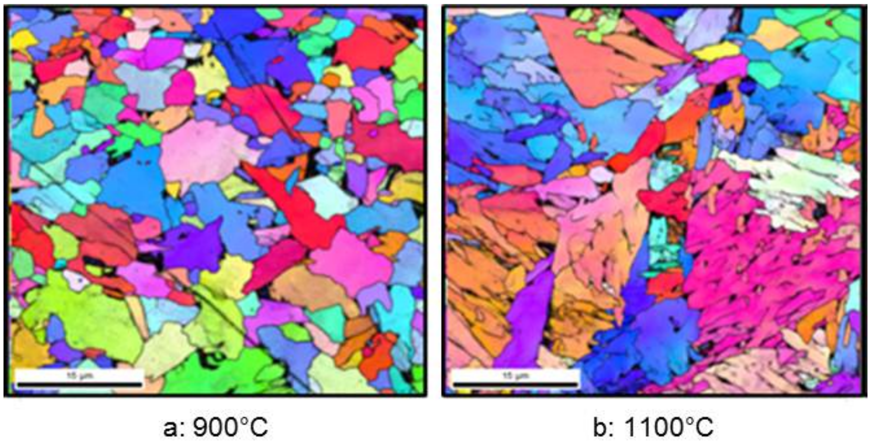

a: 900°C

b: 1100°C

Figure 4-3: Comparison of Hot Torsion Peak Temperatures

4.2.2.2 Cooling Rate

Figure 4-4 shows EBSD scans of Gleeble samples #7 (SCD) and #6 (2^k DOE) that had a difference in cooling rates of 95°C/s: peak temperatures (1050°C and 1100°C respectively), strain and strain-rates were held constant. An increase in cooling rate of 95°C/s resulted in a 66% increase aspect ratio and a 70% decrease in HAGB.

The increase in lath ferrite with increasing cooling rate is likely a function of PAG size and undercooling. In HSLA steels, accelerated cooling rates limit diffusion, which have been found to produce a more refined lath structure as illustrated by continuous cooling transformation (CCT) diagrams [9]. This is attributed a higher degree of undercooling, which is particularly prevalent the larger the PAG size [50].

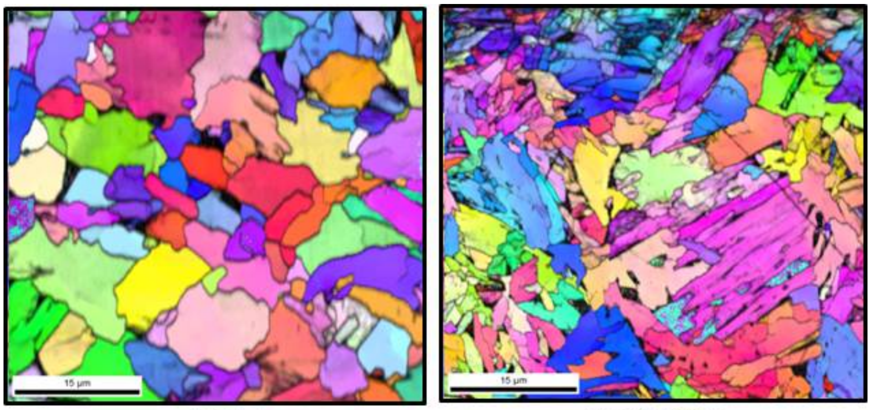

a: 15°C/s b: 110°C/s

Figure 4-4: Comparison of Hot Torsion Cooling Rates

Gleeble samples were successful in simulating microstructures found in the weld HZ. Analysis indicates that peak temperature and cooling rate are the primary factors that affect the formation of lath ferrite. Strain and strain-rate were found to have no effect on microstructural characteristics. TA_3 was largely dependent upon the peak temperature and cooling rate. Therefore, a simple thermal process should produce similar results.

4.3 Jominy Quench

Jominy quench tests were successful in simulating a wide range of microstructures over a range of peak temperatures and cooling rates. Figure 4-5 shows EBSD scans from several Jominy samples at different peak temperatures and cooling rates. These show a range of microstructures, from largely polygonal (Figure 4-5c) to 94% lath ferrite (Figure 4-5a). The range of peak temperatures and cooling rates tested these microstructures are consistent with typical CCT diagrams for this material [51].

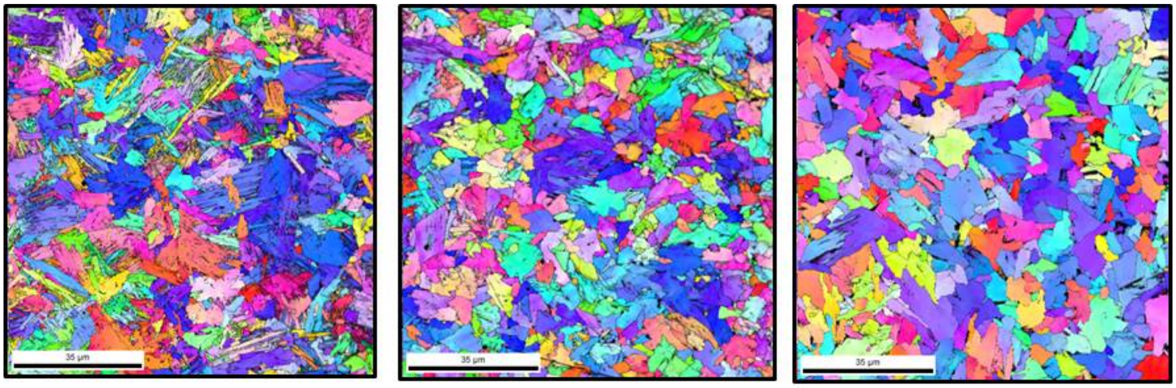

a: Jominy 1100°C – 312°C/s   b: Jominy 900°C – 136°C/s   c: Jominy 1000°C – 45°C/s

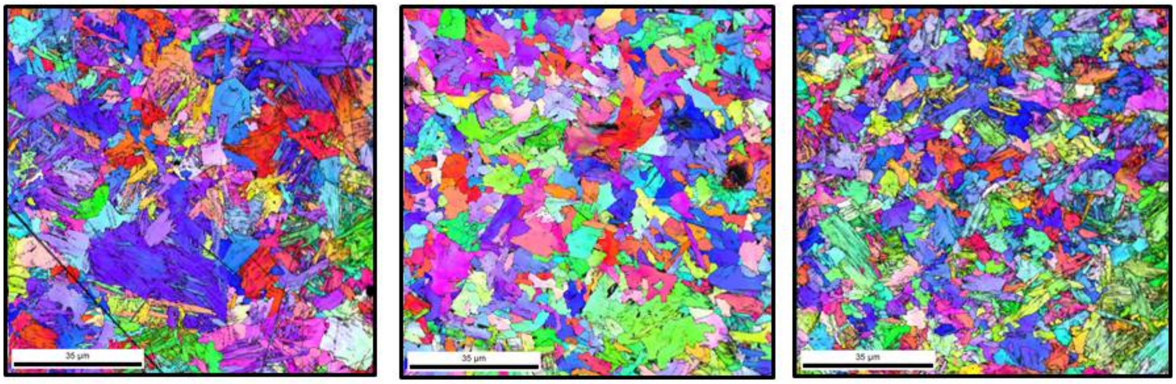

d: Jominy 1100°C – 237°C/s   e: Jominy 1000°C – 237°C/s   f: Jominy 900°C – 237°C/s

Figure 4-5: Jominy Microstructure Comparison

Results from the quantitative microstructural analysis of Jominy samples are found in Table 4-4. This data was used to create a surface plot of aspect ratio as a function of peak temperature and cooling rate (Figure 4-6). As mentioned, in this study aspect ratio was effective in identifying changes in lath structures. The surface plot is useful in understanding changes in aspect ratio, which is an indication of changes in lath structures, but does not describe the exact type of microstructure.

Table 4-4: Jominy End Quench Results

Cooling Rate (°C/s)	Aspect Ratio		
	900	1000	1100
312	2.72	2.54	3.06
237	2.6	2.51	2.85
136	2.35	2.39	2.5
45	2.29	2.39	2.36

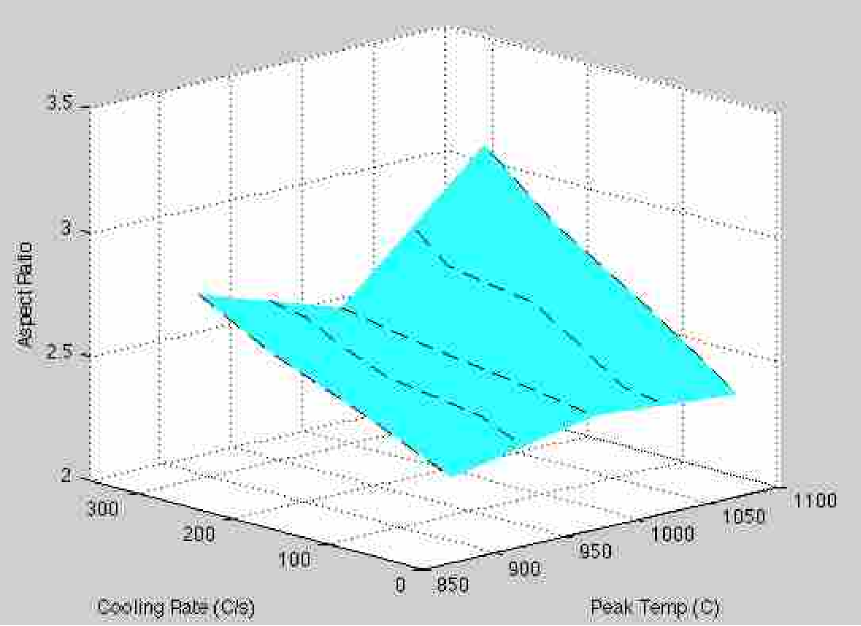

Figure 4-6: Interpolated Surface Plot Jominy Aspect Ratio

From Figure 4-6, aspect ratio increases with both increasing peak temperature and cooling rate. With respect to aspect ratio, cooling rate has an average slope of 1.0 (45°) and peak temperature has an average slope of 0.37 (20°). This is indication that cooling rate has a greater influence on aspect ratio.

The 1000°C sample had a lower slope in relation to the 900 and 1100°C samples. To eliminate any possible experimental complications, this test temperature was repeated several times resulting in similar data. The 1000°C sample results were accepted as accurate, but the mechanisms of this occurrence are not investigated further in this study.

Jominy tests with cooling rates greater than 136°C/s exhibited lath ferrite that closely resemble lath structures found in the weld HZ. At higher cooling rates, all Jominy peak temperatures resulted in primarily lath ferrite (Figure 4-5d-f) that have aspect ratios (Table 4-4) similar to weld HZ aspect ratios (Table 4-2).

Successful simulation of the weld HZ microstructure in Jominy tests further confirms Gleeble findings. Both Jominy and Gleeble data show lath ferrite formations in X65 are largely a result of peak temperature and accelerated cooling rates.

4.4 **Weld HZ Formation**

The HZ is generally a localized region on the AS of the weld. Figure 4-7a is an illustration of the transition in weld microstructure observed in FSW HSLA steel. The HZ is typically a localized region no larger than 1mm^2 in area and the transition from lath ferrite to polygonal ferrite in the SZ occurs over relatively short distances (0.5-2mm [8]).

Given the results presented in this study, the rapid transition to lath ferrite indicates that peak temperature and/or cooling rate must be higher on the AS of the weld. Previous work has shown differences in peak temperature between the AS and RS. Nelson et al. reported in FSW of HSLA steel that HAZ temperatures on the AS were approximately 20°C hotter than the RS [8]. Nandan concluded the temperature on the AS is approximately 40°C higher [52].

In FSW of HSLA steel, the difference in peak temperature from the AS to RS is likely not large enough to cause the observed variations in microstructure. When comparing FSW to the Gleeble and Jominy results of this study, 40°C had little effect on lath ferrite microstructure. Therefore, cooling rate must be the dominant factor affecting the weld HZ.

Cooling rates in the weld HZ can be estimated by comparing HZ microstructures to similar microstructures in Jominy testing. The transition from lath to polygonal ferrite in the weld from HZ to SZ (Figure 4-7a) is similar to the transition in microstructure in Jominy testing that occurred over a range of 4-8 mm (Figure 4-7b). The difference in cooling rate over this distance ranges from 237-43°C/s. This indicates that there is at least an estimated 150°C/s difference in cooling rates on the AS of the weld.

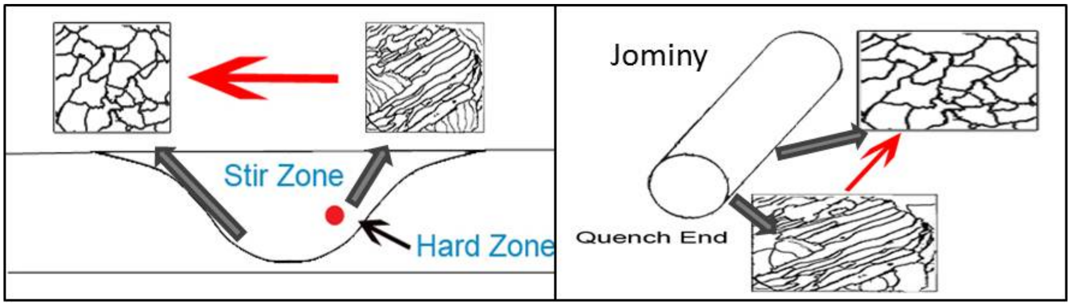

a: Weld Microstructure Transition b: Jominy Microstructure Transition

Figure 4-7: Microstructural Evolution FSW X65 vs. Jominy Quench

Accelerated cooling rates on the AS are best explained by comparing FSW to a traditional milling process. Payton and others used this model to predict peak temperatures in FSW [53,54]. It is also useful to help explain the increase in cooling rate on the AS of the weld.

In conventional milling a majority of the heat generated in the shear zone is removed by the chip, leaving the workpiece relatively cool in comparison (Figure 4-8c). Referring to Figure 4-8a and b, material on the AS of a FSW is removed similar to a conventional milling process. Material on the RS is removed similar to a climb milling process (Figure 4-8b).

Similar to conventional milling, as material from the AS is removed a majority of heat is carried away with the extruded material, leaving the base metal relatively cool. The removed material is extruded around the tool, and then redeposited on the cooler AS [24-28, 55]. When the extruded material comes in contact with the cooler base metal it results in an immediate quench. The resultant accelerated cooling rates would produce an increase in lath ferrite.

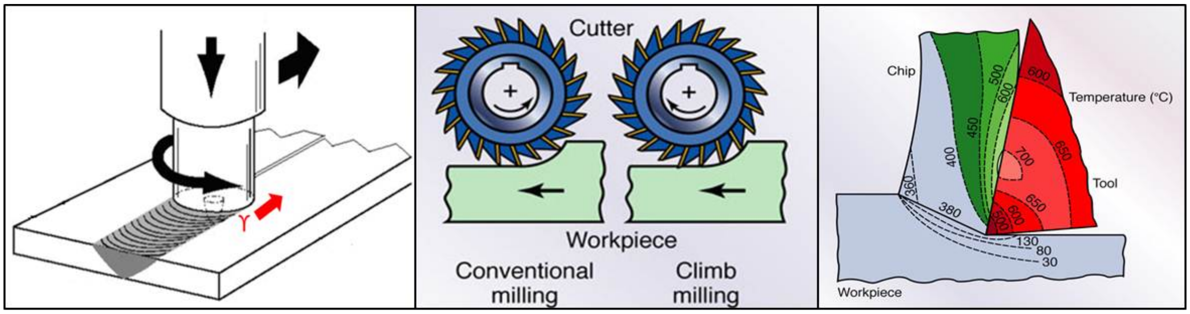

a: FSW Tool Rotation/Advancing b: Traditional Milling/Cutting [8] c: Chip-Tool Interface Thermal Profile [8]

Figure 4-8: FSW Compared to Conventional Cutting Process

4.5 Effects of Weld Parameters

The Jominy results presented in this study indicate that a given aspect ratio could be attained via a combination of peak temperatures and cooling rates. In Figure 4-9, the weld HZ aspect ratios (Table 4-2) have been superimposed on the Jominy results presented in Figure 4-5. This plot indicates that it is possible to achieve HZ aspect ratios from a number of combinations of peak temperatures and cooling rates.

However, in FSW, peak temperatures and cooling rates are dependent variables and the relationship between these dependent variables and FSW parameters are not well understood.

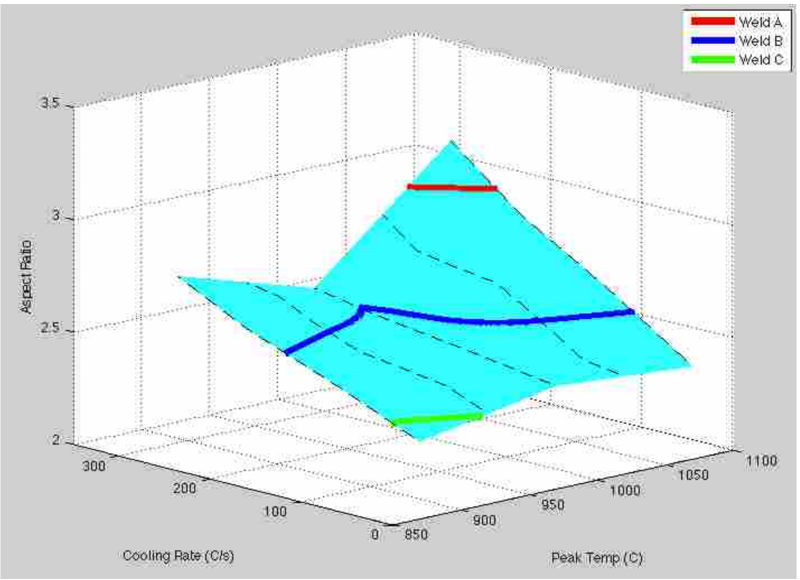

Figure 4-9: Interpolated Surface Plot of Jominy Aspect Ratio w/ Weld HZ Aspect Ratio

It is generally accepted that in FSW, cooling rates and peak temperature are largely dependent on weld parameters. Reynolds reported correlation between weld power and peak temperature [56] and cooling rate has been found to correlate to weld travel speed [57,58].

Cooling rate is also largely dependent on surrounding the environment, which includes both active and passive systems. Active systems such as pre and post process air or laser heating/cooling have been found to effectively alter cooling rate [59-61]. Passive systems such as changes in anvil material have been found to affect weld cooling rates and even reported reductions in the HZ in HSLA steels [62].

To reduce the formation of lath ferrite in the weld HZ, it would require finite control of thermal variables and their interactions during FSW. Currently, there has not been a comprehensive study investigating the relationship between weld power, travel speed, weld environment, peak temperatures and cooling rates.

A majority of current research has focused on understanding correlations between weld parameters and post-weld microstructure or the use of modeling to simulate the effects of weld parameters. Many of the models involve numerical simulations that include strain and strain-rate in addition to thermal variables. Studying the effects of post-weld microstructures only provides an understanding of weld parameters, without understanding the underlying cause of microstructural development.

The findings of this study may provide insight for future research of microstructural formations in FSW of HSLA steels. As was discussed, the HZ of FSW X65 predominantly consists of lath ferrite which results in a decrease in toughness. Though FSW is a highly plastic deformation process, lath ferrite in the HZ is primarily a result of accelerated cooling rates and peak temperature.

Focusing future research and modeling on understanding how weld parameters affect peak temperature and more importantly cooling rates will provide a means to possibly eliminating the weld HZ. Further, this knowledge could be expanded into understanding how to control the overall weld microstructure to achieve desired weld material properties.

5 CONCLUSIONS

The formation of the HZ was previously believed to be a combination of weld characteristics: strain, strain-rate, peak temperature, cooling rate. In this study each of these weld characteristics were investigated and evaluated using known thermo-mechanical and thermal processes. The following conclusions can be made of X65 material:

1. Gleeble and Jominy testing were both successful in simulating microstructures observed in the HZ of FSW X65.
2. For strain and strain-rate from 1 to 2, and 0.12 to 1.19sec^{-1} respectively, both strain and strain-rate were found to have no influence on the formation of lath ferrite in X65 HSLA steel. Statistical analysis of strain and strain-rate resulted in p-values greater than 0.19 and 0.18 (respectively), indicating that both variables have no effect on the microstructural morphology of HSLA X65.
3. Peak temperature and cooling rate were found to be the most influential factors on lath ferrite formation in X65. In Gleeble testing, a 22% increase in peak temperature and a 367% increase in cooling rate resulted in a 73% increase in lath ferrite aspect ratio. In Jominy testing, cooling rate was found to have a 270% greater influence on lath ferrite aspect ratio than peak temperature.

4. The HZ on the AS of FSW X65 was found to be a direct result of accelerated cooling rates. Analysis of comparable microstructures in Jominy testing indicates that cooling rates on the AS could be as much as 150°C/s higher than rest of the weld.
5. Given current understanding of FSW, a decrease in IPM at constant power and/or RPM would lead to reduction (or possible elimination) of the HZ in FSW X65.

REFERENCES

[1] "High-Strength Structural and High-Strength Low-Alloy Steels," in *ASM Metals Handbook*. vol. 1, 10 ed: ASM International, 1990, pp. 389-415.

[2] A. Ozekcin, H. Jin, J. Koo, N. Bangaru, R. Ayer, G. Vaughn*, et al.*, "A Microstructural Study of Friction Stir Welded Joints of Carbon Steels," *International Journal of Offshore and Polar Engineering,* vol. 14, 2004.

[3] Y. Sato, T. Nelson, C. Sterling, R. Steel, and C. Pettersson, "Microstructure and mechanical properties of friction stir welded SAF 2507 super duplex stainless steel," *Materials Science and Engineering: A,* vol. 397, pp. 376-384, 2005.

[4] J. Defalco, "Friction stir process now welds steel pipe," *The Welding J,* vol. 88, pp. 44-48, 2009.

[5] T. Santos, T. Hermenegildo, C. Afonso, R. Marinho, M. Paes, and A. Ramirez, "Fracture toughness of ISO 3183 X80M (API 5L X80) steel friction stir welds," *Engineering Fracture Mechanics,* vol. 77, pp. 2937-2945, 2010.

[6] Y. Lee, J. Kim, J. Lee, K. Kim, J. Koo, and D. Kwon, "Using the instrumented indentation technique for stress characterization of friction stir-welded API X80 steel," *Philosophical Magazine,* vol. 86, pp. 5497-5504, 2006.

[7] A. Fragiel, R. Schouwenaarf, R. Guardián, and R. Pérez, "Microstructural characteristics of different commercially available API 5L X65 steels," *Journal of New Materials for Electrochemical Systems,* vol. 8, pp. 115-119, 2005.

[8] T. Nelson, S. Anderson, and D. Segrera, "Friction Stir Welding of X-65," *TMS,* vol. Friction Stir Welding and Processing IV, 2007.

[9] H. Bhadeshia and R. Honeycombe "Hardenability and heat treatment," in *Steels microstructure and properties*, 3 ed: Elsevier Ltd., 2006, pp. 173-181.

[10] G. Spanos, R. Fonda, R. Vandermeer, and A. Matuszeski, *Microstructural changes in HSLA-100 steel thermally cycled to simulate the heat-affected zone during welding*. New York, NY, ETATS-UNIS: Springer, 1995.

[11] D. Viano, N. Ahmed, and G. Schumann, "Influence of heat input and travel speed on microstructure and mechanical properties of double tandem submerged arc high strength low alloy steel weldments," *Science and Technology of Welding & Joining,* vol. 5, pp. 26-34, 2000.

[12] K. Prasad and D. Dwivedi, "Some investigations on microstructure and mechanical properties of submerged arc welded HSLA steel joints," *The International Journal of Advanced Manufacturing Technology,* vol. 36, pp. 475-483, 2008.

[13] T. Lienert, W. Stellwag Jr, B. Grimmett, and R. Warke, "Friction stir welding studies on mild steel," *WELDING JOURNAL-NEW YORK-,* vol. 82, p. 1, 2003.

[14] L. Wei, "Investigating correlations of microstructures, mechanical properties and FSW process variables in friction stir welded high strength low alloy 65 steel," Brigham Young University, 2010.

[15] S. Sanderson and T. Nelson, "Effect of Processing Parameters on Friction Stir Welded HSLA-65 Charpy V-Notch Impact Toughness," *Friction Stir Welding and Processing VI,* pp. 19-24, 2011.

[16] M. Wade and A. Reynolds, "Friction stir weld nugget temperature asymmetry," *Science and Technology of Welding &# 38; Joining,* vol. 15, pp. 64-69, 2010.

[17] H. Schmidt and J. Hattel "Thermal Modeling in Friction Stir Welding," *Scripta materialia,* vol. 58, pp. 332-337, 2008.

[18] A. Nunes, E. Bernstein, and J. McClure, "A rotating plug model for friction stir welding," 2000.

[19] Z. Zhang and J. Chen, "The simulation of material behaviors in friction stir welding process by using rate-dependent constitutive model," *Journal of Materials Science,* vol. 43, pp. 222-232, 2008.

[20] G. Buffa and L. Fratini, "Friction stir welding of steels: process design through continuum based FEM model," *Science and Technology of Welding &# 38; Joining,* vol. 14, pp. 239-246, 2009.

[21] M. Matsushita, Y. Kitani, R. Ikeda, and S. Endo, "Microstructure and Toughness of Friction Stir Weld of 12 mm Thick Structural Steel," in *International Offshore and Polar Engineering Conference*, Maui, Hawaii, USA, 2011.

[22] M. Sinfield, "Advancements in Physical Simulation and Thermal History Acquisition Techniques for Ferrous Alloy Friction Stir Welding," Ohio State University, 2007.

[23] A. Pilchak, W. Tang, H. Sahiner, A. Reynolds, and J. Williams, "Microstructure Evolution during Friction Stir Welding of Mill-Annealed Ti-6Al-4V," *Metallurgical and Materials Transactions A,* vol. 42, pp. 745-762, 2011.

[24] T. Seidel and A. Reynolds, "Visualization of the material flow in AA2195 friction-stir welds using a marker insert technique," *Metallurgical and materials Transactions A,* vol. 32, pp. 2879-2884, 2001.

[25] B. Liechty and B. Webb, "Modeling the frictional boundary condition in friction stir welding," *International Journal of Machine Tools and Manufacture,* vol. 48, pp. 1474-1485, 2008.

[26] R. Nandan, G. Roy, T. Lienert, and T. Debroy, "Three-dimensional heat and material flow during friction stir welding of mild steel," *Acta Materialia,* vol. 55, pp. 883-895, 2007.

[27] P. Ulysse, "Three-dimensional modeling of the friction stir-welding process," *International Journal of Machine Tools and Manufacture,* vol. 42, pp. 1549-1557, 2002.

[28] W. Arbegast, "Modeling friction stir joining as a metalworking process," *Hot deformation of aluminum alloys,* vol. 3, p. 313, 2003.

[29] T. Lienert, R. Grylls, J. Gould, and H. Fraser, "Deformation microstructures in friction stir welds on 6061-T651," *Proceedings of Hot Deformation of Aluminum Alloys,* pp. 159-167, 1998.

[30] M. Mahoney, C. Rhodes, J. Flintoff, W. Bingel, and R. Spurling, "Properties of friction-stir-welded 7075 T651 aluminum," *Metallurgical and Materials Transactions A,* vol. 29, pp. 1955-1964, 1998.

[31] P. Konkol, J. Mathers, R. Johnson, and J. Pickens, "Friction stir welding of HSLA-65 steel for shipbuilding," *Journal of ship production,* vol. 19, pp. 159-164, 2003.

[32] J. Cho, D. Boyce, and P. Dawson, "Modelling of strain hardening during friction stir welding of stainless steel," *Modelling and Simulation in Materials Science and Engineering,* vol. 15, p. 469, 2007.

[33] Y. Zhang, Y. Sato, H. Kokawa, S. Park, and S. Hirano, "Microstructure and Mechanical Properties of Friction Stir Welded Ti-15V-3Al-3Cr-3Sn Alloy," in *Trends in Welding Research: Proceedings of the 8th International Conference, June 1-6, 2008, Callaway Gardens Resort, Pine Mountain, Georgia, USA*, 2009, p. 413.

[34] K. Sampath, "An understanding of HSLA-65 plate steels," *Journal of materials engineering and performance,* vol. 15, pp. 32-40, 2006.

[35] M. Zhao, K. Yang, and Y. Shan, "The effects of thermo-mechanical control process on microstructures and mechanical properties of a commercial pipeline steel," *Materials Science and Engineering: A,* vol. 335, pp. 14-20, 2002.

[36] S. Das, A. Ghosh, S. Chatterjee, and P. Rao, "The effect of cooling rate on structure and properties of a HSLA forging," *Scripta materialia,* vol. 48, pp. 51-57, 2003.

[37] C. Wang, M. Wang, J. Shi, W. Hui, and H. Dong, "Effect of microstructure refinement on the strength and toughness of low alloy martensitic steel," *Journal of Materials Science and Technology-Shenyang,* vol. 23, p. 659, 2007.

[38] H. Fujii, L. Cui, N. Tsuji, M. Maeda, K. Nakata, and K. Nogi, "Friction stir welding of carbon steels," *Materials Science and Engineering: A,* vol. 429, pp. 50-57, 2006.

[39] S. Norton, *Ferrous friction stir weld physical simulation*, Ohio State University, 2006.

[40] D. Forrest and M. Sinfield, "Numerical Simulation of Gleeble Torsion Testing of HSLA-65 Steel," DTIC Document, 2008.

[41] ASTM, "Standard Test Methods for Determining Hardenability of Steel," in *ASTM International*, ed. West Conshohocken, PA, 2007.

[42] G. Totten and M. Howes, *Steel heat treatment handbook*: CRC Press, 1997.

[43] W. Jominy and A. Boegehold, "A hardenability test for carburizing steel," *Trans. ASM,* vol. 26, pp. 574-606, 1938.

[44] S. Thompson, D. Colvin, and G. Krauss, "Austenite decomposition during continuous cooling of an HSLA-80 plate steel," *Metallurgical and Materials Transactions A,* vol. 27, pp. 1557-1571, 1996.

[45] T. Gladman, *The Physical Metallurgy of Microalloyed Steels*. London: The Institute of Materials, 1997.

[46] S. Dhua, "Studies on influence of reheating temperature and cooling rate on structure-property behaviour of lean chemistry HSLA-100 steel," *Materials Science and Technology,* vol. 27, pp. 1377-1384, 2011.

[47] E. Metzbower, G. Spanos, R. Fonda, and R. Vandermeer, "Prediction of microstructure and properties in the heat affected zone of HSLA-100 weldments," *Science and Technology of Welding & Joining,* vol. 2, pp. 27-32, 1997.

[48] A. Bakkaloğlu, "Effect of processing parameters on the microstructure and properties of an Nb microalloyed steel," *Materials Letters,* vol. 56, pp. 263-272, 2002.

[49] M. Shome, O. Gupta, and O. Mohanty, "Effect of simulated thermal cycles on the microstructure of the heat-affected zone in HSLA-80 and HSLA-100 steel plates," *Metallurgical and materials Transactions A,* vol. 35, pp. 985-996, 2004.

[50] M. Korchynsky, "A new role for microalloyed steels-adding economic value," in *Proceedings of Vanitec International Symposium*, 2001, pp. 13-14.

[51] N. Enzinger and H. Cerjak, "Welding of High Strength Steel in Hydropower Applications–the Cleuson-Dixence Case," 2009.

[52] R. Nandan, G. Roy, T. Lienert, and T. DebRoy, "Numerical modelling of 3D plastic flow and heat transfer during friction stir welding of stainless steel," *Science and Technology of Welding & Joining,* vol. 11, pp. 526-537, 2006.

[53] L. Fratini, G. Buffa, D. Palmeri, J. Hua, and R. Shivpuri, "Material flow in FSW of AA7075&# 8211; T6 butt joints: numerical simulations and experimental verifications," *Science and Technology of Welding & Joining,* vol. 11, pp. 412-421, 2006.

[54] L. Payton, "Metal Cutting Theory and Friction Stir Welding," *Trends in Welding Research: Proceedings of the 7th International Conference, May 16-20, Pine Mountain, Georgia, USA*, 2005, p. 257.

[55] T. Seidel and A. Reynolds, "Two-dimensional friction stir welding process model based on fluid mechanics," *Science and Technology of Welding & Joining,* vol. 8, pp. 175-183, 2003.

[56] A. Reynolds, W. Tang, T. Gnaupel-Herold, and H. Prask, "Structure, properties, and residual stress of 304L stainless steel friction stir welds," *Scripta Materialia,* vol. 48, pp. 1289-1294, 2003.

[57] R. Mishra and Z. Ma, "Friction stir welding and processing," *Materials Science and Engineering: R: Reports,* vol. 50, pp. 1-78, 2005.

[58] R. Nandan, T. DebRoy, and H. Bhadeshia, "Recent advances in friction-stir welding – Process, weldment structure and properties," *Progress in Materials Science,* vol. 53, pp. 980-1023, 2008.

[59] G. Kohn, "Improved process and apparatus for friction stir welding," ed: WO Patent 2,002,074,479, 2002.

[60] O. Grong, A. O. Kluken, and O. Midling, "Modified friction stir welding," ed: WO Patent App. PCT/NO1999/000,042, 1999.

[61] L. Fratini, G. Buffa, and R. Shivpuri, "In-process heat treatments to improve FS-welded butt joints," *The International Journal of Advanced Manufacturing Technology,* vol. 43, pp. 664-670, 2009.

[62] S. Rose, "The Effect of Cooling Rate on Friction Stir Welded HSLA Steel," Brigham Young University, 2013.

APPENDIX A: ENGINEERING DRAWING SPECIFICATIONS

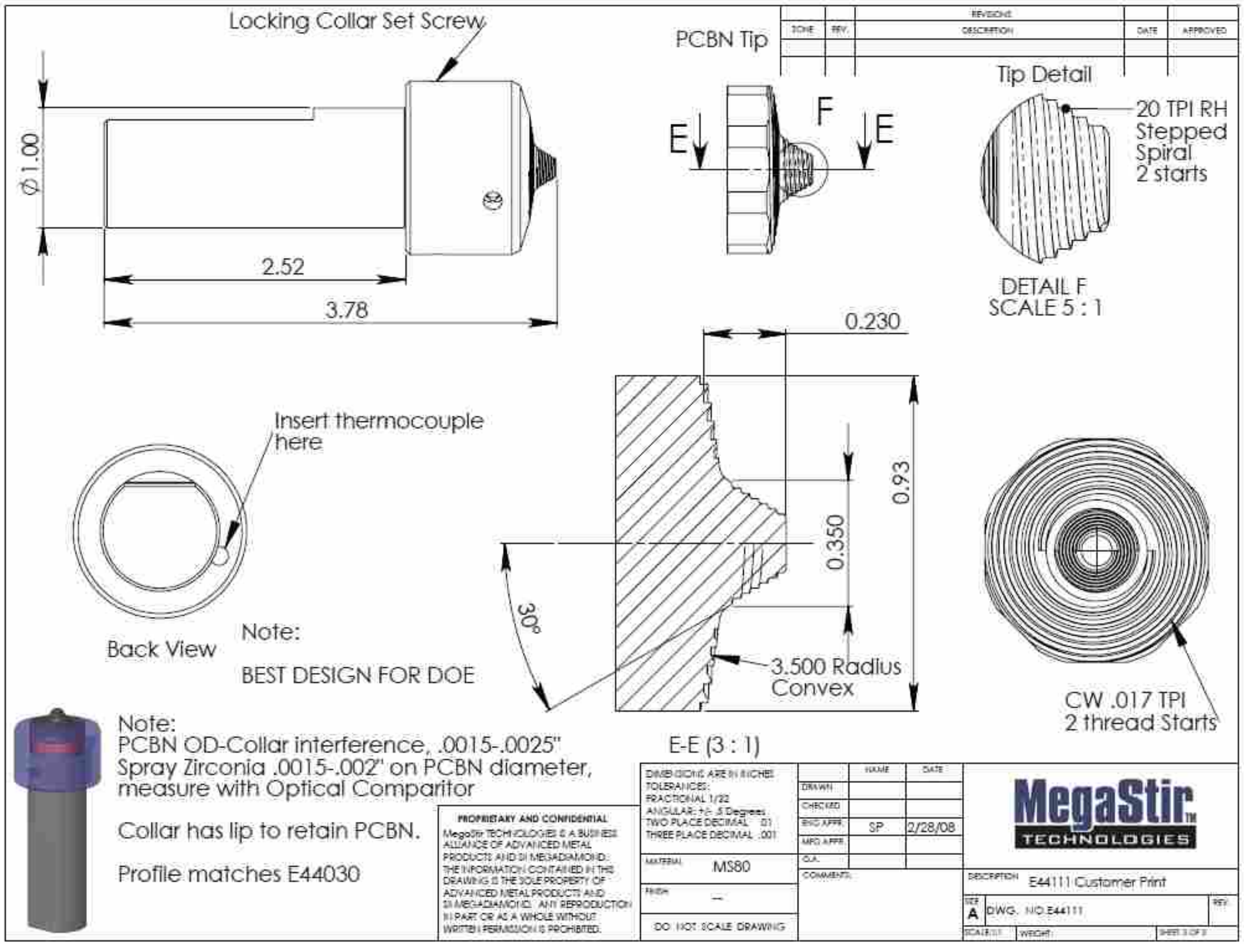

Figure A-1: CS4 Tool Design

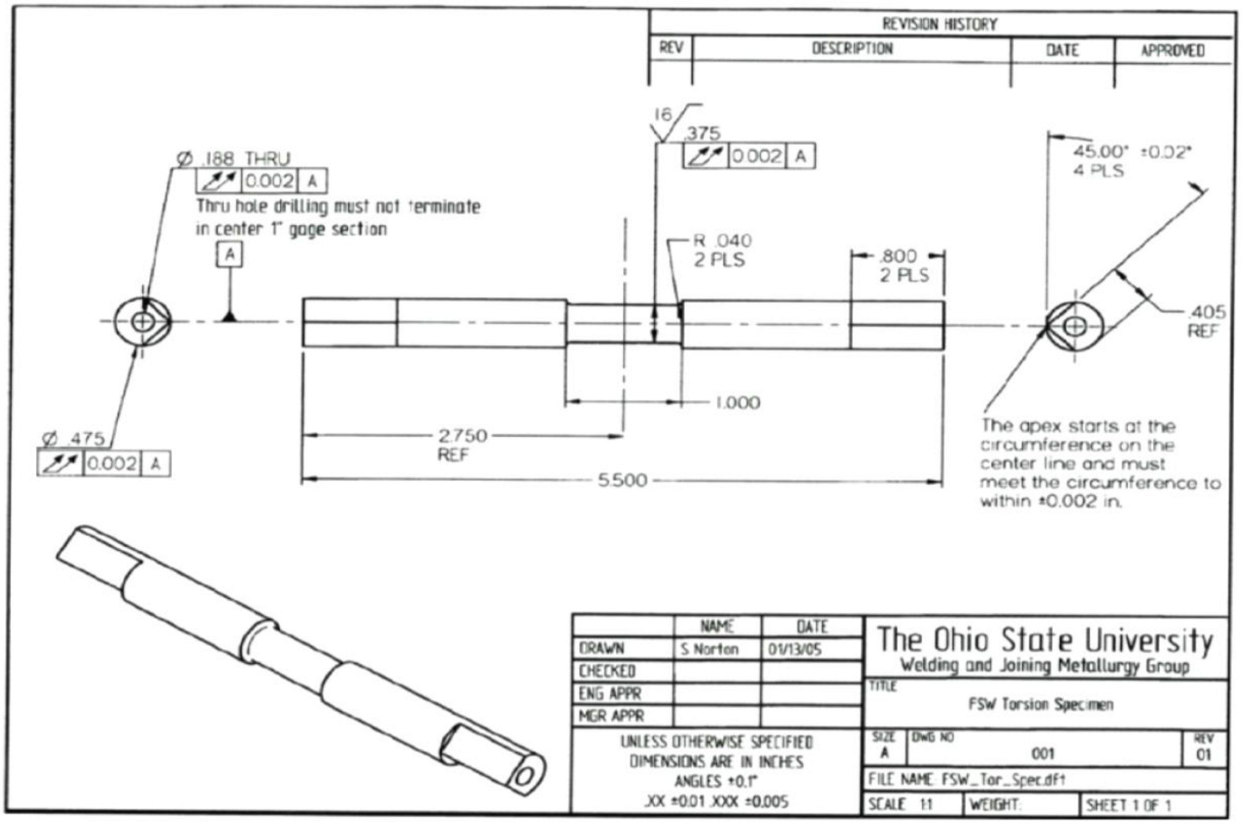

Figure A-2: Modified Gleeble Specimen [39]

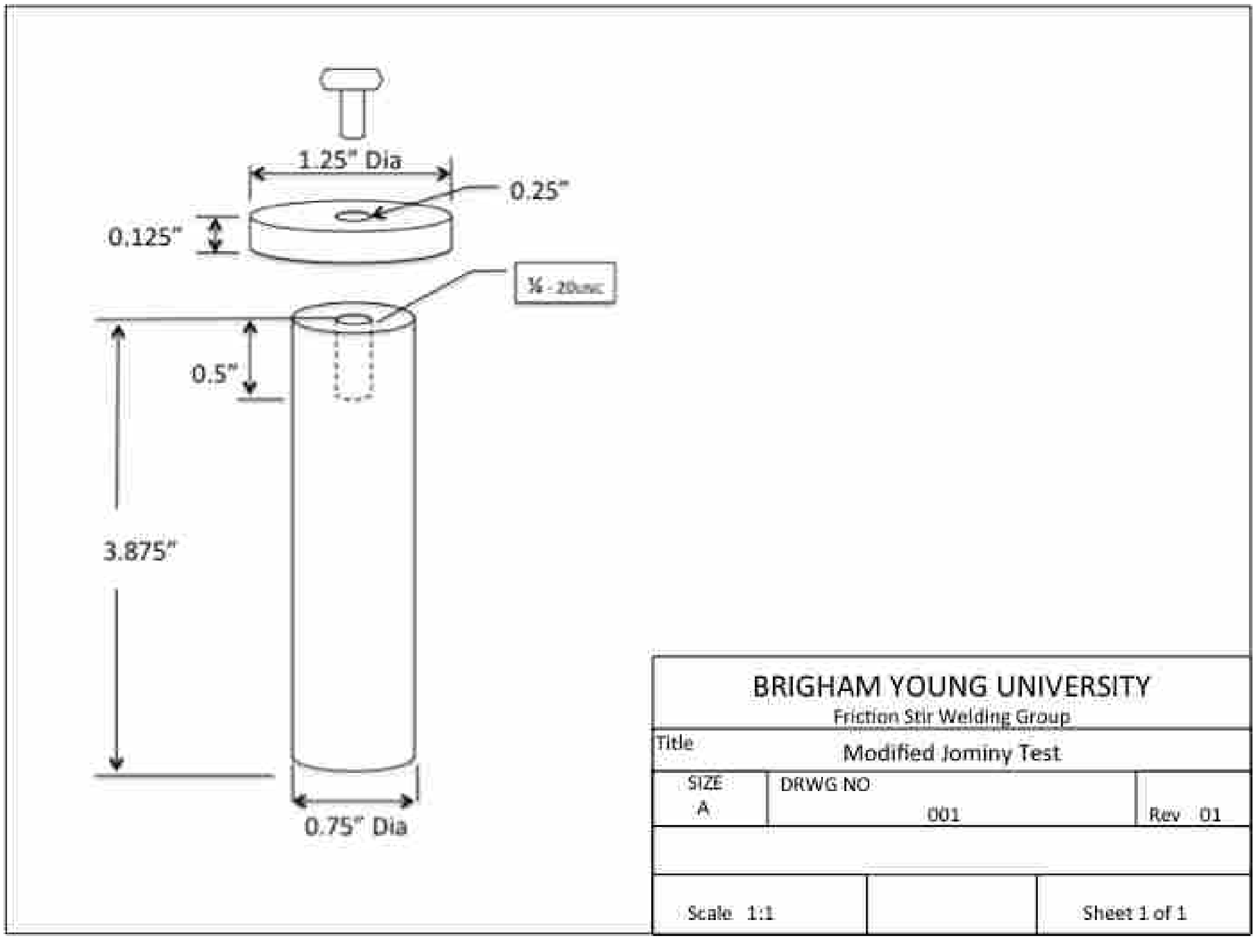

Figure A-3: Modified Jominy End Quench Test

APPENDIX B: EXPERIMENTAL TESTING SPECIFICATIONS

Table B-1: Small Composite Design Experiment

Pattern	Temperature (°C)	Strain	Strain Rate	Cooling Rate (He PSI)
0	950	1.5	0.6565	20
+++−	1000	1.75	0.925	10
000a	950	1.5	0.6565	0
000A	950	1.5	0.6565	40
−+−+	900	1.75	.388	30
−−+−	900	1.25	0.925	10
A000	1050	1.5	0.6565	20
0A00	950	2	0.6565	20
0a00	950	1	0.6565	20
00a0	950	1.5	0.119	20
++++	1000	1.75	0.925	30
−−++	900	1.25	0.925	30
00A0	950	1.5	1.194	20
0	950	1.5	0.6565	20
+−−+	1000	1.25	.388	30
−+−−	900	1.75	.388	10
+−−−	1000	1.25	.388	10
a000	850	1.5	0.6565	20

Table B-2: 2^k Experimental Design

Temperature (°C)	Cooling Rate (°C/s)	Time Above A_3 (sec)
915	55	300
1110	64	9.8
1102	126	300
905	31	10
904	27	300
1008	45	155
1113	110	10
906	88	10
1007	62	155
1107	87	300